Research Article

Nano Research
2024, 17(3): 1140–1150

ISSN 1998-0124 CN 11-5974/O4
https://doi.org/10.1007/s12274-023-5939-9

Nitrogen incorporated oxygen vacancy enriched $MnCo_2O_x/BiVO_4$ photoanodes for efficient and stable photoelectrochemical water splitting

Liangcheng Xu[1], Yingjuan Zhang[1], Boyan Liu[1], Xin Wang[1], Gangqiang Zhu[2] (✉), Lianzhou Wang[3] (✉), Songcan Wang[1,4] (✉), and Wei Huang[1] (✉)

[1] *Frontiers Science Center for Flexible Electronics, Xi'an Institute of Flexible Electronics (IFE), Northwestern Polytechnical University, 127 West Youyi Road, Xi'an 710072, China*
[2] *School of Physics and Information Technology, Shaanxi Normal University, Xi'an 710062, China*
[3] *Nanomaterials Centre, Australian Institute for Bioengineering and Nanotechnology and School of Chemical Engineering, The University of Queensland, Brisbane, Queensland 4072, Australia*
[4] *Research & Development Institute of Northwestern Polytechnical University in Shenzhen, Sanhang Science & Technology Building, No. 45th, Gaoxin South 9th Road, Nanshan District, Shenzhen 518063, China*

Received: 14 May 2023 / **Revised:** 14 June 2023 / **Accepted:** 18 June 2023

ABSTRACT

Oxygen vacancies in oxygen evolution cocatalysts (OECs) can significantly improve the photoelectrochemical (PEC) water splitting performance of photoanodes. However, OECs with abundant oxygen vacancies have a poor stability when exposing to the highly-oxidizing photogenerated holes. Herein, we partly fill oxygen vacancies in a $MnCo_2O_x$ OEC with N atoms by a combined electrodeposition and sol-gel method, which dramatically improves both photocurrent density and stability of a $BiVO_4$ photoanode. The optimized N filled oxygen vacancy-rich $MnCo_2O_x/BiVO_4$ photoanode (3 at.% of N) exhibits an outstanding photocurrent density of 6.5 mA·cm^{-2} at 1.23 V_{RHE} under AM 1.5 G illumination (100 mW·cm^{-2}), and an excellent stability of over 150 h. Systematic characterizations and theoretical calculations demonstrate that N atoms stabilize the defect structure and modulate the surface electron distribution, which significantly enhances the stability and further increases the photocurrent density. Meanwhile, other heteroatoms such as carbon, phosphorus, and sulfur are confirmed to have similar effects on improving PEC water splitting performance of photoanodes.

KEYWORDS

water splitting, oxygen evolution, bismuth vanadate ($BiVO_4$), filling oxygen vacancies, cocatalysts

1 Introduction

Photoelectrochemical (PEC) water splitting that can convert solar energy into hydrogen has attracted increasing attention in the past decades [1–3]. It is well known that oxygen evolution reaction (OER) on the photoanode is a critical and limiting factor for overall water splitting due to its sluggish four-electron transfer compared to a facile two-electron transfer of hydrogen evolution reaction (HER) on a photocathode [4–6]. Therefore, the development of efficient photoanode materials is essential for high-performance PEC water splitting. Bismuth vanadate ($BiVO_4$) has been regarded as a promising photoanode material due to its narrow bandgap (2.4 eV) for visible light absorption, proper band-edge position for oxygen evolution, and high theoretical solar-to-hydrogen conversion (STH) efficiency (9.2%) under AM 1.5 G illumination (100 mW·cm^{-2}) [7–9]. However, the relatively short hole diffusion length and sluggish surface OER kinetics result in severe electron–hole recombination in the bulk and surfaces of the $BiVO_4$ photoanodes [10–12]. In the past few years, some effective strategies including doping element [13], constructing heterojunction [14–16], controlling morphology [17, 18] as well as loading oxygen evolution cocatalysts (OECs) [19–23] have been developed to address the above mentioned intrinsic issues. Despite the excellent charge separation efficiencies in the bulk of $BiVO_4$ photoanodes achieved by various strategies, modification of the $BiVO_4$ surfaces with an outstanding OEC to accelerate the OER kinetics is indispensable for efficient PEC water oxidation [24–26].

Recently, creating oxygen vacancies in OECs has been considered as a smart strategy to further improve surface OER kinetics and interface charge transport in photoanodes. For instance, abundant oxygen vacancies in an ultrathin and crystalline β-FeOOH OEC provided enough diving force for hole transfer at the β-FeOOH/electrolyte interface and decreased recombination of electron–hole pairs, leading to a photocurrent density of 4.3 mA·cm^{-2} at 1.23 V vs. reversible hydrogen electrode (RHE) and a negative shift of onset potential by 100–200 mV for a β-FeOOH/$BiVO_4$ photoanode [27]. It was found that oxygen vacancies could activate OECs and provide highly-active sites for OER process. Oxygen vacancies were constructed in a Co_3O_4 OEC

Address correspondence to Songcan Wang, iamscwang@nwpu.edu.cn; Wei Huang, iamwhuang@nwpu.edu.cn; Gangqiang Zhu, zgq2006@snnu.edu.cn; Lianzhou Wang, l.wang@uq.edu.au

by facile Ar-plasma bombardment, achieving an excellent photocurrent density that is nearly two times higher than its untreated counterpart [28]. Other OECs such as $Ni_{1-x}Fe_xS$ [29] and $Fe_2(MoO_4)_3$ [30] with oxygen vacancies also exhibited higher water oxidation performance compared to their untreated counterparts. However, oxygen vacancies in OECs are not stable under a highly-oxidizing OER process due to the hole accumulation at the OECs/electrolyte interface [31], resulting in poor stability. How to stabilize oxygen vacancies in OECs is critical to achieve high-performance photoanodes while challenging.

Nitrogen possesses lone-pair electrons in 2p orbitals, which is a good candidate to fill oxygen vacancies in OECs to modulate their electronic structures and adsorption properties, thus boosting the PEC performance of the photoanodes. Herein, we partly fill oxygen vacancies in $MnCo_2O_x$ OECs with N atoms by a combined electrodeposition and sol-gel method in $MnCo_2O_x/BiVO_4$ photoanodes, which is effective to achieve both excellent photocurrent densities and stability. Via accurately controlling the N atomic ratio from 1 at.% to 10 at.%, we found that the $MnCo_2O_x/BiVO_4$ photoanode with 3 at.% of N filling the oxygen vacancies in the $MnCo_2O_x$ OEC (N filled $MnCo_2O_x/BiVO_4$ (N:MCB)) exhibits an outstanding photocurrent density of 6.5 mA·cm^{-2} at 1.23 V vs. RHE, which is 270% and 135% higher than that of the pristine $BiVO_4$ photoanode (2.4 mA·cm^{-2}) and untreated $MnCo_2O_x/BiVO_4$ photoanode (4.8 mA·cm^{-2}), respectively. The photocurrent density achieved in this work is at the top of the state-of-the-art OECs/$BiVO_4$ photoanodes (Table S1 in the Electronic Supplementary Material (ESM)). In addition, the optimized N:MCB photoanode has a stability of over 150 h upon consecutive AM 1.5 G illumination for PEC water splitting, while obvious decay of the photocurrent density is observed for the untreated oxygen vacancy-rich $MnCo_2O_x/BiVO_4$ photoanode within 1 h. Theoretical calculations have demonstrated that N atoms make electron cloud enrich around the Co active sites and change the adsorption properties in OER process. The formed N–Mn bonds can stabilize oxygen vacancies at defect sites, thus improving the stability performance during PEC water splitting. In addition, owing to the intrinsic attraction between the negative charged electrons and the positive charged holes, the electron enriched Co sites can significantly extract photogenerated holes from the $BiVO_4$ photoanodes for OER, suppressing interfacial charge recombination. Furthermore, we confirmed that other heteroatoms such as carbon, phosphorus, and sulfur have similar effects to increase the PEC water splitting performance of $MnCo_2O_x/BiVO_4$ photoanodes. The new findings demonstrated in this work will inspire the design of efficient photoanodes for solar fuel production.

2 Experimental

2.1 Preparation of $BiVO_4$ films on the fluorinated tin oxide (FTO) glass

The preparation of $BiVO_4$ film was based on a previous report with some modifications [32]. Firstly, 3.32 g of KI was dissolved in deionized water (50 mL), and pH of the solution was adjusted to 1.7 by adding HNO_3. Then, 0.49 g of $Bi(NO_3)_3$ was added into the KI solution under ultrasonication. In addition, 0.495 g of p-benzoquinone was dissolved in 20 mL of absolute ethyl alcohol and mixed with a KI solution containing $Bi(NO_3)_3$ to prepare the electrolyte. The preparation of BiOI was based on the three-electrode system by electrodeposition. In this system, a clean FTO glass, an Ag/AgCl (4 M KCl) electrode, and platinum wire electrode were used as working electrode (WE), reference electrode (RE), and counter electrode (CE), respectively. Meanwhile, the deposited voltage and deposited time were controlled in −0.1 V (vs. RHE) and 240 s. Finally, 0.1 mL of dimethyl sulfoxide (DMSO) solution containing 0.0265 g of vanadyl acetylacetonate ($VO(acac)_2$) was dropped on the prepared BiOI film, followed by heating in a muffle furnace at 500 °C for 2 h (heating rate: 2 °C·min^{-1}).

2.2 Preparation of oxygen vacancy-rich $MnCo_2O_x/BiVO_4$ films by an electrodeposition method

The preparation of oxygen vacancy-rich $MnCo_2O_x$ particles on nanoporous $BiVO_4$ film (denoted as BVO) was based on a simple electrodeposition method under negative potential. The employed three-electrode system was identical to the preparation process of BiOI film. For the compound of electrolyte, $Co(NO_3)_2·6H_2O$ (10 mM) and different amounts of $Mn(NO_3)_2·6H_2O$ (5 mM) were dissolved in 70 mL of deionized water under sufficient stirring. To explore the optimized experimental conditions, the different deposited voltage (−0.25, −0.5, and −0.75 V vs. Ag/AgCl) and different deposited time (5, 10, and 20 s) were employed for electrodeposition. Finally, the prepared $MnCo(OH)_x$/BVO photoanodes were annealed in a muffle furnace at 500 °C for 2 h (heating rate: 2 °C·min^{-1}) to obtain the oxygen vacancy-rich $MnCo_2O_x/BiVO_4$ photoanodes.

2.3 Preparation of N:$MnCo_2O_x/BiVO_4$ films by a combined electrodeposition and sol-gel method

The N-filled oxygen vacancy-rich $MnCo_2O_x$ catalyst was successfully synthesized by a sol-gel method using an ion solution containing Mn^{2+}, Co^{2+} as well as NO_3^-. Firstly, 1 g of polyvinyl pyrrolidone (PVA) was dissolved in 10 mL of isopropyl alcohol under sufficient stirring to obtain a sol solution. Then, the ion solution was obtained by dissolving 5 mM of $Co(NO_3)_2·6H_2O$ and 2.5 mM of $Mn(NO_3)_2·6H_2O$ into 5 mL of deionized water at 80 °C. After that, the precursor solution was prepared by mixing the sol solution and ion solution, which was spin-coated on the oxygen vacancy-rich $MnCo_2O_x/BiVO_4$ photoanode to fill oxygen vacancies with N atoms. Finally, the N:$MnCo_2O_x/BiVO_4$ films were annealed at 500 °C for 2 h (heating rate: 2 °C ·min^{-1}).

2.4 Preparation of C:$MnCo_2O_x/BiVO_4$, S:$MnCo_2O_x/BiVO_4$, and P:$MnCo_2O_x/BiVO_4$ films by a combined electrodeposition and sol-gel method

Other non-metallic heteroatoms such as carbon (C), sulfur (S), and phosphorus (P) were also filled into the oxygen vacancy-rich $MnCo_2O_x$ catalyst by similar synthesis methods. The difference is that, for the C:$MnCo_2O_x/BiVO_4$, the ion solution contained 5 mM of sucrose and 5 mL of deionized water; for the S:$MnCo_2O_x/BiVO_4$, the ion solution contained 5 mM of manganese sulfate and 5 mL of deionized water; and for the P:$MnCo_2O_x/BiVO_4$, the ion solution contained 5 mM of disodium hydrogen phosphate and 5 mL of deionized water. The remaining synthesis procedures were identical to the preparation of the N:$MnCo_2O_x/BiVO_4$ films.

2.5 Preparation of pristine oxygen vacancy-rich $MnCo_2O_x$ film on FTO glass by electrodeposition method

To obtain the $MnCo_2O_x$ film on FTO glass, the electrodeposition method under negative potential was applied to the preparation process. The FTO substrates as the working electrodes were immersed in an electrolyte containing 10 mM of $Co(NO_3)_2·6H_2O$, 5 mM of $Mn(NO_3)_2·6H_2O$ as well as 70 mL of deionized water. The deposited voltages and deposited time were set as −1 V vs. Ag/AgCl and 15 s, respectively. Then, the prepared $MnCo(OH)_x$

film was annealed in a muffle furnace at 500 °C for 2 h (heating rate: 2 °C·min^{-1}) to obtain a pristine oxygen vacancy-rich $MnCo_2O_x$ film on FTO glass.

2.6 Characterizations

The certain morphology of photoanode surface and cross-section were carried out via field-emission scanning electron microscopy (FE-SEM). The specific crystal structure and surface element composition were obtained by X-ray diffraction (XRD) and high-resolution transmission electron microscopy (HRTEM). The surface chemical state was performed by X-ray photoelectron spectroscopy (XPS). The light absorption capability of photoanodes was characterized by ultraviolet–visible (UV–vis) spectroscopy. The recombination intensity of photo-generated electron–hole pairs as well as carrier lifetime were measured by photoluminescence (PL) technology with laser excitation at 356 nm (10 Hz full width at half maximum (FWHM) ~ 7 ns) and the time-resolved transient absorption (TRTA) technology. In addition, the carrier lifetime dependent on the decay time curves was fitted by a biexponential decay model.

2.7 Photoelectrochemical measurements

The PEC measurements were carried out by using an electrochemical station (CHI 760E, Chen Hua China) with a three electrodes system, where the photoanodes acted as working electrodes; the Ag/AgCl (4 M KCl) electrode acted as the reference electrode; platinum wire acted as the counter electrode. The light source of AM 1.5 G solar illumination (100 mW·cm^{-2}) was provided by a Xenon lamp (CEL-NP2000-2A) equipped with an AM 1.5 G filter, and the back illumination was utilized for all photoelectrochemical measurements. Meanwhile, the linear sweep voltammetry (LSV) measurements, electrochemical impedance spectroscopy (EIS) measurements, cyclic voltammetry (CV) measurements, and chronoamperometry (*i*–*t*) measurements were conducted in a 0.5 M borate buffer solution (adjusting the pH up to 9.5 by using potassium hydroxide) under AM 1.5 G solar illumination at room temperature (approximately 25 °C). For the charge separation efficiency measurements at the electrode surface, 0.5 M of sodium sulfite (Na_2SO_3) as a hole scavenger was added to the borate buffer electrolyte. Additionally, the measured potential and frequency ranges of EIS curves were set as 1.23 V_{RHE} and 10^{-2} to 10^5 Hz, respectively. The potential versus Ag/AgCl was converted into reversible hydrogen electrode potential (E_{RHE}) by the following Nernst equation [33]

$$E_{RHE} = E_{Ag/Agcl} + 0.059 \times pH + 0.197 \quad (1)$$

where E_{RHE} is the translated potential from $E_{Ag/AgCl}$, and $E_{Ag/AgCl}$ is obtained by practical experimental results.

In the incident photon to current efficiency (IPCE) measurements, the monochromator of a Xenon lamp from 375 to 520 nm wavelength was applied to the LSV measurements to obtain the IPCE curves, and the corresponding calculated equation as follows [34]

$$IPCE(\%) = \frac{1240 \times J\,(mA \cdot cm^{-2})}{P_{light} \times \lambda\,(nm)} \times 100\% \quad (2)$$

where J is the photocurrent density at a specific wavelength; P_{light} is the light intensity of a monochromator; λ is the wavelength.

The applied bias photon to current (ABPE) efficiencies could be obtained by the following equation [35]

$$ABPE = \frac{J_{H_2O} \times (1.23V - V_{app})}{P_{light}} \times 100\% \quad (3)$$

where J_{H_2O} is the photocurrent density obtained by the LSV curves; V_{app} is the corresponding potential (0 V_{RHE} to 1.23 V_{RHE}); and P_{light} is the simulated solar power (100 mW·cm^{-2}).

The Faradaic efficiency was calculated using following equations [36]

$$\text{Faradaic efficiency} = \frac{\text{Experimental gas yields}}{\text{Theoretical gas yields}} \times 100\% \quad (4)$$

$$\text{Theoretical gas yields} = \frac{I \times t}{Z \times F} \times 100 \quad (5)$$

where I is photocurrent (A); t is time (s); Z is the amount of transferred electrons (Z = 4 for O_2, Z = 2 for H_2); and F is the Faradaic constant (96,485 C·mol^{-1}).

The relative electrochemical active surface area (ECSA) of BVO and N:MCB is calculated by the following equation [37]

$$ECSA \propto C_{dl} = \frac{\frac{dQ}{dt}}{\frac{dE}{dt}} = \frac{i(E)}{v} \quad (6)$$

where C_{dl} represents the double-layer capacitances; $i(E)$ is the current density at a dark condition; and v is the scan rate varying from 20 to 100 mV·s^{-1}.

The average carrier lifetime of different samples could be calculated by the following equation [38]

$$\tau_{avg} = \frac{A_1\tau_1^2 + A_2\tau_2^2}{A_1\tau_1 + A_2\tau_2} \quad (7)$$

where the A and τ are fitting parameters of the TRTA kinetic based on a biexponential decay model.

The minority carrier diffusion length (L_D) based on average carrier lifetime is obtained as follows [39]

$$L_D = (D\tau)^{\frac{1}{2}} \quad (8)$$

where D is the diffusion coefficient, and τ is the average carrier lifetime.

The surface charge injection efficiency ($P_{injection}$) was achieved with and without Na_2SO_3 electrolyte respectively by the following equation [40]

$$P_{injection} = \frac{J_{H_2O}}{J_{Na_2SO_3}} \times 100\% \quad (9)$$

where the J_{H_2O} is measured in 0.5 M borate buffer solution (pH = 9.5); $J_{Na_2SO_3}$ is measured in 0.5 M sodium sulfite (Na_2SO_3) electrolyte; and the above applied potential changes from 0 V_{RHE} to 1.3 V_{RHE}.

2.8 Computational method

We employed the Vienna *ab initio* package (VASP) [41] to perform all the spin-polarized density functional theory (DFT) calculations within the generalized gradient approximation (GGA) using the Perdew–Burke–Ernzerhof (PBE) [42] formulation. We chose the projected augmented wave (PAW) potentials [43] to describe the ionic cores and take valence electrons into account using a plane wave basis set with a kinetic energy cutoff of 400 eV. Partial occupancies of the Kohn–Sham orbitals were allowed using the Gaussian smearing method and a width of 0.05 eV. The electronic energy was considered self-consistent when the energy change was smaller than 10^{-5} eV. A geometry optimization was considered convergent when the force change was smaller than 0.02 eV·Å^{-1}. Grimme's DFT-D3 [44] methodology was used to describe the dispersion interactions.

The equilibrium lattice constant of spinel-type $MnCo_2O_4$ unit cell was optimized, when using a 4 × 4 × 4 Monkhorst–Pack *k*-point grid for Brillouin zone sampling, to be a = 8.570 Å. We then

used it to construct a $MnCo_2O_4$(311) surface model with p (1 × 1) periodicity in the x and y directions and 3 stoichiometric layers in the z direction separated by a vacuum layer in the depth of 15 Å in order to separate the surface slab from its periodic duplicates. This model comprised of 12 Mn, 24 Co, and 48 O atoms. One O atom on the outmost layer was removed to build model 1 and one O atom was replaced by N to build model 2. During structural optimizations, the gamma point in the Brillouin zone was used for k-point sampling, and the bottom two stoichiometric layers were fixed while the top one was allowed to relax.

The adsorption energy (E_{ads}) of adsorbate A is defined as

$$E_{ads} = E_{A/surf} - E_{surf} - E_{A(g)} \quad (10)$$

where $E_{A/surf}$, E_{surf}, and $E_{A(g)}$ are the energy of adsorbate A adsorbed on the surface, the energy of clean surface, and the energy of isolated A molecule in a cubic periodic box with a side length of 20 Å and a 1 × 1 × 1 Monkhorst–Pack k-point grid for Brillouin zone sampling, respectively.

The free energy of a gas phase molecule or an adsorbate on the surface was calculated by the equation $G = E + ZPE - TS$, where E is the total energy; ZPE is the zero-point energy; T is the temperature in kelvin (298.15 K is set here); and S is the entropy.

3 Results and discussion

As shown in Fig. 1(a), BVO films were prepared on fluorine-doped SnO_2 (FTO) glass substrates according to a previous report with some modifications [45], and N-filled oxygen vacancy-rich $MnCo_2O_x$ OECs were grown on the surfaces of the obtained BVO films by a combined electrodeposition and sol-gel method to tune the electron distribution at the Co active sites, which will increase the driving force for hole extraction. The obtained pristine BVO film exhibits a worm-like morphology with an average size of 200–300 nm, and the surface particles are relatively smooth (Fig. 1(b)). The film thickness is approximately 1 μm (inset in Fig. 1(b)). Since nanoporous BVO films have been confirmed to exhibit excellent charge separation efficiencies [32], modification of the BVO surfaces with a proper OEC is essential to further improve its PEC water splitting activity and stability. An oxygen vacancy-rich $MnCo_2O_x$ cocatalyst was decorated on the BVO film by an electrodeposition process with a negative potential. The morphologies and PEC water splitting performances of the obtained $MnCo_2O_x$/BVO photoanodes can be controlled by tuning the applied potential, the molar ratio of Mn:Co, and the electrodeposition time (Figs. S1–S6 in the ESM). According to the PEC water splitting activity, the optimized conditions for the

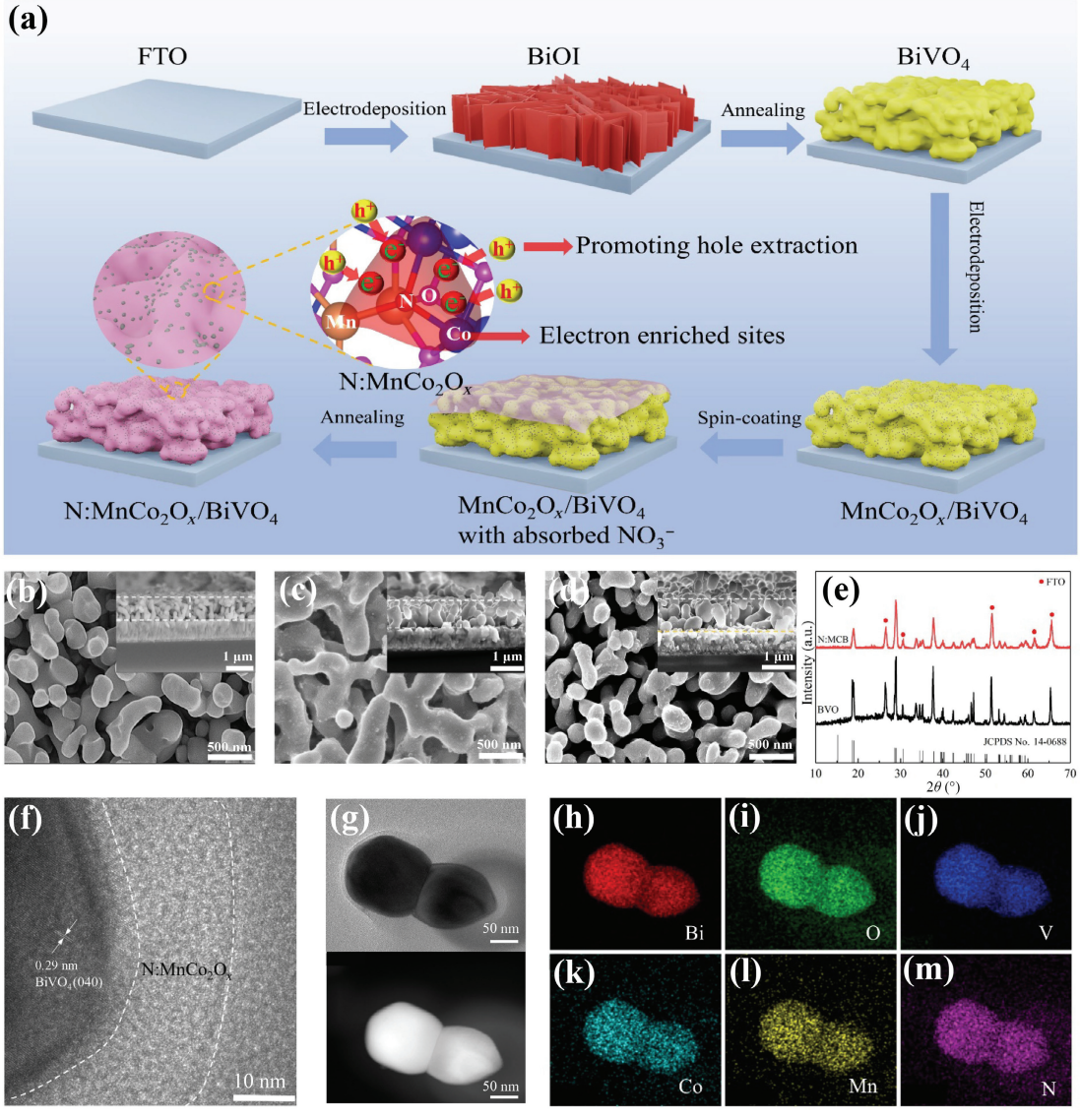

Figure 1 Preparation and characterization of the BVO, MCB, and N:MCB samples. (a) Schematic illustration for the preparation of the N:MCB samples. SEM images of the (b) BVO, (c) MCB, and (d) N:MCB samples (insets in (b)–(d)): the corresponding cross-sectional views). (e) XRD patterns of the BVO and N:MCB samples. (f) and (g) The HRTEM image and ((h)–(m)) EDS elemental mapping images of N:MCB.

preparation of a $MnCo_2O_x$ OEC are as follows: the applied potential (−0.5 V vs. RHE), the molar ratio of Mn:Co (1:2), and the electrodeposition time (10 s). Hereafter, the $MnCo_2O_x$/BVO photoanode prepared by the optimized conditions is denoted as MCB.

It can be observed that numerous $MnCo_2O_x$ nanoparticles are homogeneously and densely decorated on the surfaces of the BVO particles (Fig. 1(c)). Compared to the BVO film, no obvious changes in the film thickness can be observed (inset in Fig. 1(c)). Interestingly, we found that proper N filling in the $MnCo_2O_x$ OEC can significantly enhance the PEC water splitting performance of the MCB samples without changing their morphologies, and the optimized content of N atomic ratio is 3 at.% (Figs. S7 and S8 in the ESM). In addition, the XPS spectra of various N atomic ratios from 3 at.% to 10 at.% are shown in Figs. S7(d)–S7(f) in the ESM, and the N contents relative to $MnCo_2O_x$ and C 1s (Table S2 in the ESM) are close to the stated N atomic ratios. The optimized N-filling MCB photoanode is denoted as N:MCB. Fig. 1(d) reveals that N-filling has negligible effects on both morphology and film thickness.

The crystal structures of BVO, MCB, and N:MCB samples were characterized by XRD measurements, and the corresponding XRD patterns are shown in Fig. 1(e). The characteristic diffraction peaks of monoclinic BVO and FTO are indexed to JCPDS PDF#14-0688 and JCPDS PDF#41-1445, respectively, indicating the successful preparation of BVO photoanodes. Compared to the BVO sample, no additional peaks are observed in the XRD pattern of the N:MCB sample, possibly due to the low-content and ultrathin thickness of the oxygen vacancy-rich $MnCo_2O_x$ OEC layer. HRTEM was applied to further demonstrate the element composition and morphology structure of the N:MCB sample. As revealed in Fig. 1(f), the lattice spacing of 0.29 nm can be indexed to the (040) crystal plane of the monoclinic BVO [46]. However, the surface $MnCo_2O_x$ OEC does not show any clear lattice spacing in the HRTEM image, implying the amorphous crystal structure. The thickness of the oxygen vacancy-rich $MnCo_2O_x$ OEC is approximately 10 nm. The energy dispersive spectroscopy (EDS) elemental mapping of two connected particles (Fig. 1(g)) demonstrates the homogeneous distribution of the Bi, O, V, Co, Mn, and N elements (Figs. 1(h)–1(m)), confirming the successful synthesis of the N-filled $MnCo_2O_x$ catalyst. In addition, the characteristic peaks in the Raman spectra of BVO, MCB, and N:MCB (Fig. S9 in the ESM) can be indexed to BVO [47], and no additional peaks are observed, suggesting that the loading of $MnCo_2O_x$ and N-filled $MnCo_2O_x$ OEC do not have obvious effects on the crystal structure of BVO.

PEC performances of the BVO, MCB, and N:MCB samples were measured in a boric buffer electrolyte (pH = 9.5) under AM 1.5 G illumination (100 mW·cm^{-2}). As shown in Figs. 2(a) and 2(b), pristine BVO only exhibits a moderate photocurrent density of 2.4 mA·cm^{-2} at 1.23 V vs. RHE. With the surface deposition of an oxygen vacancy-rich $MnCo_2O_x$ OEC, the photocurrent density of the MCB sample is significantly increased to 4.8 mA·cm^{-2} at 1.23 V vs. RHE. Surprisingly, the photocurrent density of the N:MCB sample is further boosted to 6.5 mA·cm^{-2} at 1.23 V vs. RHE when the surface $MnCo_2O_x$ OEC is filled with 3 at.% of N, which is at the top of the state-of-the-art BVO/OEC photoanodes (Table S1 in the ESM). To confirm the effect of N-filling in oxygen vacancies on the PEC water splitting performance of the N:MCB samples, another solution containing only Mn^{2+} and Co^{2+} (without NO_3^-) was spin-coated on a MCB sample, followed by thermal treatment (details are shown in the Experimental Section), and the obtained sample was denoted as MCB (pure sol). As shown in Fig. S10(a) in the ESM, the LSV curve of the MCB (pure sol) is almost the same as that of MCB. In addition, a N-filled BVO film (denoted as N:BVO) was prepared using exactly the same process of the N:MCB by replacing the MCB sample with pristine BVO. It can be observed that the PEC water splitting performance of N:BVO is very similar to that of the pristine BVO (Fig. S10(b) in the ESM). Therefore, the effect of the spin-coating process on the PEC water splitting performance of the N:MCB samples can be ruled out. The significantly enhanced PEC water splitting performance is mainly attributed to the incorporation of N atoms in the oxygen vacancies of the $MnCo_2O_x$ OEC layer.

Furthermore, the ABPE efficiencies of the samples were calculated based on Eq. (3). N:CMB exhibits the highest ABPE value of 2.36% at 0.62 V vs. RHE (Fig. 2(c)), which is 1.5 and 7 times higher than that of MCB (1.57% at 0.63 V_{RHE}) and BVO (0.33% at 0.93 V_{RHE}), respectively. For practical applications, a BVO photoanode should have both excellent PEC water splitting activity and stability. Although oxygen vacancy-rich $MnCo_2O_x$ OEC can effectively improve the PEC water oxidation activity for

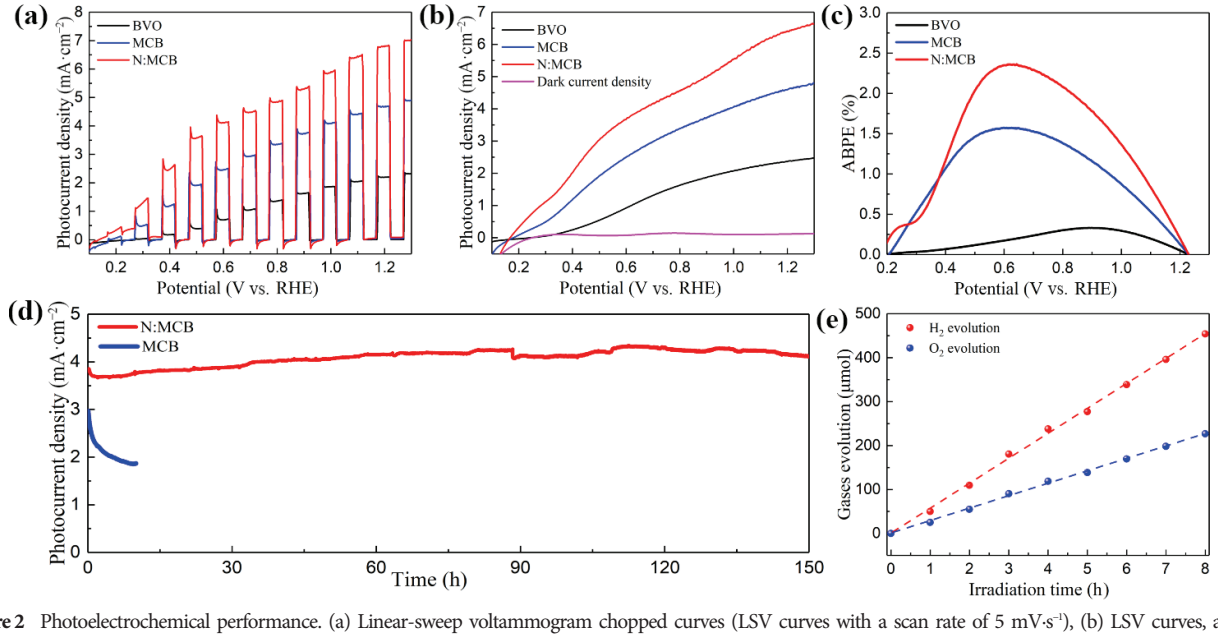

Figure 2 Photoelectrochemical performance. (a) Linear-sweep voltammogram chopped curves (LSV curves with a scan rate of 5 mV·s^{-1}), (b) LSV curves, and (c) ABPE plots of BVO, MCB, and N:MCB. (d) Stability curves at 0.6 V vs. RHE of MCB and N:MCB. (e) Gas evolution of N:MCB. A 0.5 M borate buffer solution (pH = 9.5) is used as the electrolyte for all measurements, and the light source is AM 1.5 G illumination.

BVO, its long-term stability is still an issue. As demonstrated in Fig. 2(d), the photocurrent density of MCB drops significantly from 3.0 to 2.2 mA·cm^{-2} in the initial 1.5 h, then gradually decreases to 1.8 mA·cm^{-2} after 10 h of consecutive light illumination at 0.6 V vs. RHE. Interestingly, no obvious decay in photocurrent densities is observed for its N:MCB counterpart even at 150 h (Fig. 2(d)), indicating that the incorporation of 3 at.% of N into the oxygen vacancies of the $MnCo_2O_x$ OEC can dramatically improve the PEC water splitting stability. It should be mentioned there is a slight increment of photocurrent density at the beginning of approximately 60 h, then the photocurrent density is almost stable at the rest of 90 h. The increase of photocurrent density on N:MCB can be attributed to the photothermal effect of $MnCo_2O_x$ OEC that converts near-infrared radiation under AM 1.5 G illumination into heat and increases the temperature on the electrode surfaces [48], leading to improved water oxidation kinetics.

To further confirm the excellent stability of N:MCB, SEM, XRD, and XPS were conducted to characterize the N:MCB sample after long-term stability measurement. As shown in Fig. S11(a) in the ESM, the BVO particles are still fully covered by N:MCB nanoparticles, which is similar to the as-received N:MCB sample (Fig. 1(d)). The XRD pattern of N:MCB-tested is similar to that of the as-received N:MCB and no additional peaks can be observed (Fig. S11(b) in the ESM), suggesting the excellent crystal structure stability of the N:MCB sample. XPS results confirm that the valence states of the main elements of N, Co, and Mn in N:MCB before and after long-term stability measurement are similar (Fig. S12 in the ESM), indicating the excellent chemical state stability. The gas evolution of hydrogen and oxygen within 8 h is demonstrated in Fig. 2(e), which presents a linear trend. After an 8 h gas collection, the yields of hydrogen and oxygen reach up to 514 and 257 μmol respectively, corresponding to a Faradaic efficiency of 94.1 % calculated by Eqs. (4) and (5).

To clarify the underlying mechanism of N-filled $MnCo_2O_x$ OEC for boosting the PEC water splitting activity and stability of the BVO photoanode, the optoelectronic properties of BVO, MCB, and N:MCB were systematically investigated. Interestingly, although BVO, MCB, and N:MCB exhibit a similar light absorption edge of around 520 nm (Fig. 3(a)), the light absorption intensities of MCB and N:MCB are much higher than that of BVO in the range of 300–480 nm, indicating that the $MnCo_2O_x$ OEC layer can strengthen the light absorption intensity within the bandgap of BVO. Thus, more photons can be converted to electron–hole pairs, leading to the increase of photocurrent densities in the presence of Na_2SO_3 as a hole scavenger (Fig. S13 in the ESM). In addition, the base lines of MCB and N:MCB beyond the light absorption range are higher than that of BVO, which is due to the dark color of $MnCo_2O_x$ OEC that blocks the transmittance of the incident light. The IPCE reflects the ability to convert photons into currents at a specific wavelength. As shown in Fig. 3(b), all samples exhibit IPCE values in the wavelength range of 300–520 nm, which is consistent with the UV–vis light absorption curves (Fig. 3(a)). More specifically, BVO exhibits an IPCE value of only 31% at 365 nm, whereas MCB exhibits a higher IPCE value of 55%. Impressively, the IPCE value of N:MCB is as high as 90%, which almost doubles that of MCB and triples that of BVO. Thus, N:MCB can greatly promote the conversion of incident photons into currents, resulting in higher photocurrent densities.

To evaluate the capability of charge transport at the photoanode/electrolyte interfaces, EIS curves of BVO, MCB, and N:MCB were collected. The corresponding Nyquist plots and

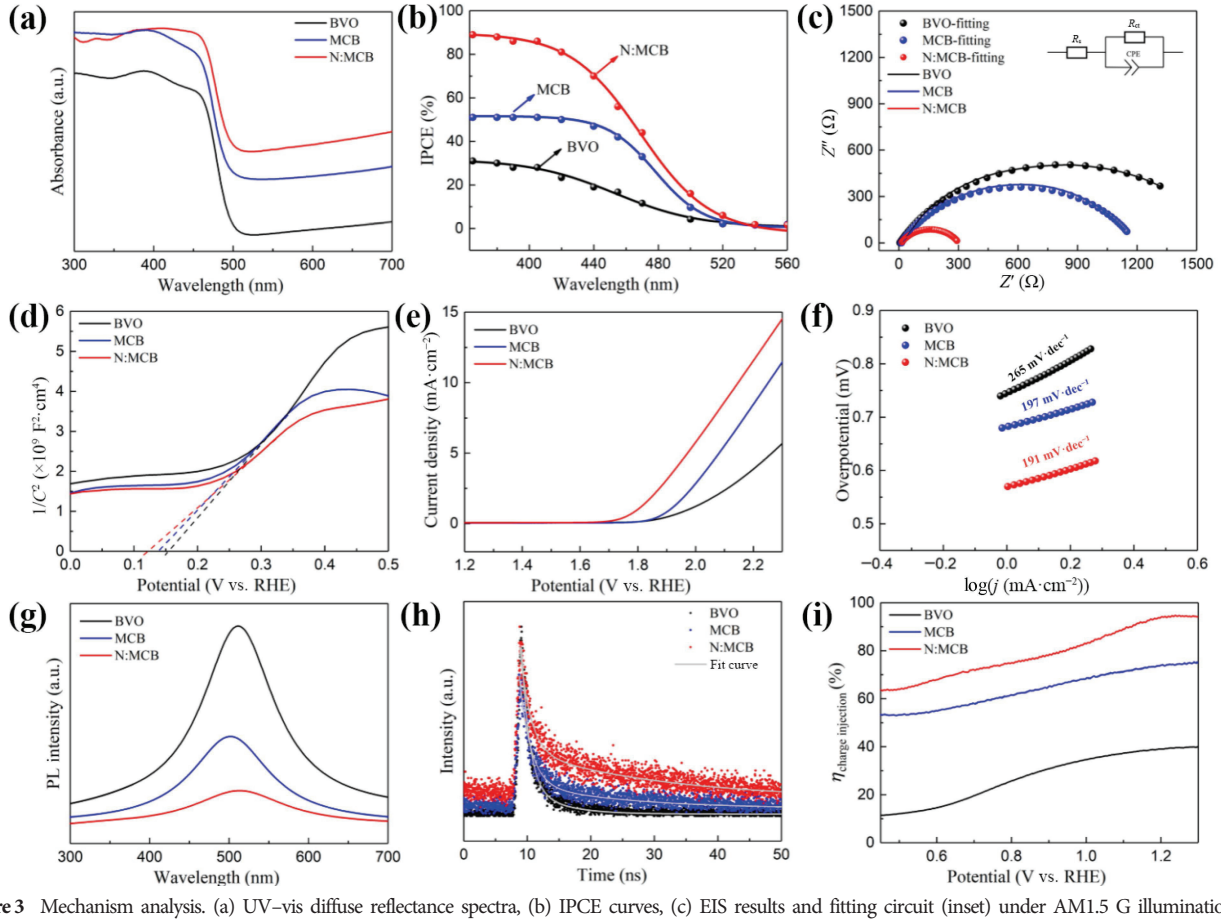

Figure 3 Mechanism analysis. (a) UV–vis diffuse reflectance spectra, (b) IPCE curves, (c) EIS results and fitting circuit (inset) under AM1.5 G illumination, (d) Mott–Schottky (M–S) plots, (e) LSV curves under dark, (f) Tafel plots, and (g) PL spectra. (h) The TRTA curves and (i) surface injection efficiencies of the BVO, MCB, and N:MCB samples.

equivalent circuit are shown in Fig. 3(c). It is obvious that the curve radius of N:MCB is much smaller than that of BVO and MCB, implying a smaller interfacial charge transfer resistance during OER [49]. To visualize the interfacial charge transfer resistance values, the Nyquist plots were fitted using the equivalent circuit (inset in Fig. 3(c)). The corresponding fitted results are listed in Table S3 in the ESM, where the R_{ct} values of BVO, MCB, and N:MCB are 1751, 1180, and 288 Ω, respectively. The fitted results suggest that the N:$MnCo_2O_x$ OEC significantly promotes the interfacial charge transfer and decreases the recombination of electrons and holes at the photoanode/electrolyte interfaces. MS plots were employed to investigate the flat band potential, the carrier concentration, and the surface status of BVO, MCB and N:MCB. As shown in Fig. 3(d), it is obvious that the loaded oxygen vacancy-rich OEC does not affect the conductive type (n-type) of BVO. However, the flat band potential of BVO is negatively shifted from 0.16 to 0.14 V vs. RHE after loaded with an oxygen vacancy-rich $MnCo_2O_x$ OEC. For N:MCB, the flat band potential is further negatively shifted to 0.12 V vs. RHE. Since $MnCo_2O_x$ is a p-type semiconductor (Fig. S14 in the ESM), these results can be ascribed to the formed p-n junction of the N:MCB that promotes the interfacial electron transfer and changes the flat-band potential (E_{FB}) [50, 51]. To evaluate the electrocatalytic performances of BVO, MCB, and N:MCB for OER, their LSV curves without light illumination were measured. As shown in Figs. 3(e) and 3(f), N:MCB exhibits a lower overpotential (1.65 V vs. RHE) and a lower Tafel slope (191 mV·dec^{-1}) in comparison to BVO (overpotential of 1.89 V vs. RHE and Tafel slope of 265 mV·dec^{-1}) and MCB (overpotential of 1.87 V vs. RHE and Tafel slope of 197 mV·dec^{-1}), implying the better electrocatalytic activity for OER [52]. The relative ECSA of BVO and N:MCB is obtained by a CV measurement (Figs. S15(a) and S15(b) in the ESM) and Eq. (6). As shown in Fig. S15(c) in the ESM, it is obvious that the double-layer capacitance (reflect the ECSA directly) of N:MCB (0.05 mF·cm^{-2}) is larger than that of BVO (0.04 mF·cm^{-2}), indicating that the loading of a $MnCo_2O_x$ OEC on the BVO surfaces could significantly improve charge transfer for OER.

To gain more insights on the enhanced PEC water splitting performance of N:MCB, the PL curves and the TRTA spectra of BVO, MCB, and N:MCB were measured. It is well known that the stronger peak intensity of a PL spectrum reflects the stronger charge recombination [53, 54]. As shown in Fig. 3(g), BVO exhibits the strongest peak intensity, while MCB exhibits a lower peak intensity in comparison to BVO, and N:MCB exhibits the lowest peak intensity. It is obvious that the PL results perfectly match the LSV curves (Fig. 2(a)), implying the suppressed surface recombination is the main reason for the enhanced PEC performance of N:MCB. The average carrier lifetime of different samples was calculated according to Eq. (7), and the results are shown in Table S4 in the ESM. It is obvious that N:MCB has a longer carrier lifetime (19.6 ns) compared to that of MCB (11.1 ns) and BVO (3.1 ns), which is another reason for the significantly enhanced PEC water splitting performance for N:MCB. Additionally, the calculated carrier lifetime values were employed to deduce the minority carrier diffusion length (L_D) using Eq. (8). The corresponding results are shown in Table S4 in the ESM, where the L_D of N:MCB reaches 49.0 nm, which is obviously higher than its BVO (19.5 nm) and MCB (36.9 nm) counterparts, suggesting a decrease carrier recombination rate on N:MCB. It should be mentioned that the L_D values calculated here may not equal to the absolute minority carrier diffusion length of the photoanodes, but the comparison between these values can reasonably reflect their charge separation and transport properties.

According to the above results, oxygen vacancy-rich $MnCo_2O_x$ as an OEC is efficient to promote water oxidation kinetics, thus suppressing the recombination of electron–hole pairs at the photoanode surfaces, leading to a significant enhancement in the PEC water splitting performance. Moreover, filling oxygen vacancies with N in the $MnCo_2O_x$ OEC can further enhance the charge injection efficiency, carrier lifetime, and carrier diffusion length. According to Eq. (9), the charge injection efficiencies of BVO, MCB, and N:MCB were calculated. BVO shows a moderate charge injection efficiency of 56% at 1.23 V vs. RHE (Fig. 3(i)). By loading an oxygen vacancy-rich $MnCo_2O_x$ OEC layer, the charge injection efficiency of MCB increases to 77%. With the fulfilment of N in the oxygen vacancy-rich $MnCo_2O_x$ OEC, the charge injection efficiency of N:MCB is drastically enhanced to 95%, indicating the N-filled oxygen vacancy-rich $MnCo_2O_x$ OEC is efficient to promote surface charge transfer for OER.

To identify the role of N-filling in the $MnCo_2O_x$ OEC for enhancing the PEC water splitting performance, XPS curves, the differential charge density, and DFT calculations of the OER reaction process of MCB and N:MCB were collected. As shown in Fig. S16 in the ESM, no evident changes of peak position could be observed in the Bi 4f and V 2p XPS spectra of MCB and N:MCB, indicating that the incorporation of N atoms has negligible effects on the chemical states of BVO. In addition, the characteristic peaks of oxygen vacancies (O_V) were detected in both MCB and N:MCB (Fig. 4(a)). Compared to the strong O_V peak in MCB, N:MCB exhibits a weaker O_V peak, which is due to the fulfilment of O_V by N atoms. To find out the bonding information between N and other metal elements in the OEC, high resolution XPS spectra of Mn 2p and Co 2p were also provided. As shown in Fig. 4(b), the Mn 2p XPS spectrum of the N:MCB presents a positive shift (0.5–1 eV) to a higher binding energy at the Mn^{2+} sites compared with the MCB, indicating the migration of partial electrons from Mn atoms to N atoms, and thereby forming N–Mn bonds [55]. It is well known that superabundant oxygen vacancies are not stable at highly-oxidizing conditions in OER. Therefore, the formed N–Mn bonds in partial oxygen vacancies will stabilize the crystalline structure of the $MnCo_2O_x$ OEC during the OER process, which is a main reason of the significantly improved stability by filling oxygen vacancies with N atoms. No evident binding energy shifts can be observed at the active sites of Co atoms (Fig. 4(c)), suggesting N atoms tend to form nitrogen–metal bonds with metal atoms with lower electronegativity instead of metal atoms with higher electronegativity [56]. Furthermore, the existence of N–Mn bonds is confirmed in Fig. S12(a) in the ESM, where the characteristic peaks of the pyrrole N (400.0 eV) and the N–Mn bonds (398.9 eV) are detected [57], implying the successful fulfillment of N atoms into the oxygen vacancy-rich $MnCo_2O_x$ and the formed N–Mn bonds at the $MnCo_2O_x$ catalyst. Therefore, the incorporation of N atoms largely changes the surface chemical states and electron structures, resulting in an excellent PEC performance.

The specific effects of N–Mn bonds at oxygen vacancy sites for OER performance are deeply investigated via DFT calculations. The theoretical models of $MnCo_2O_x$ with and without N dopants are shown in Fig. S17 in the ESM. It is obvious that the Co atoms and Mn atoms are three-fold coordinated and four-fold coordinated, respectively. The corresponding bond length of the N–Mn bonds and N–Co bonds are 1.95 and 1.88 Å, respectively. The schematic diagram of the differential charge density (Fig. 4(d)) exhibits the difference of electron density distribution induced by electron transfer when N atoms are incorporated into $MnCo_2O_x$ catalysts in which the electron densities around the N atoms have a significant enhancement (yellow regions) due to transfer of electrons from Mn atoms to N atoms. These results are

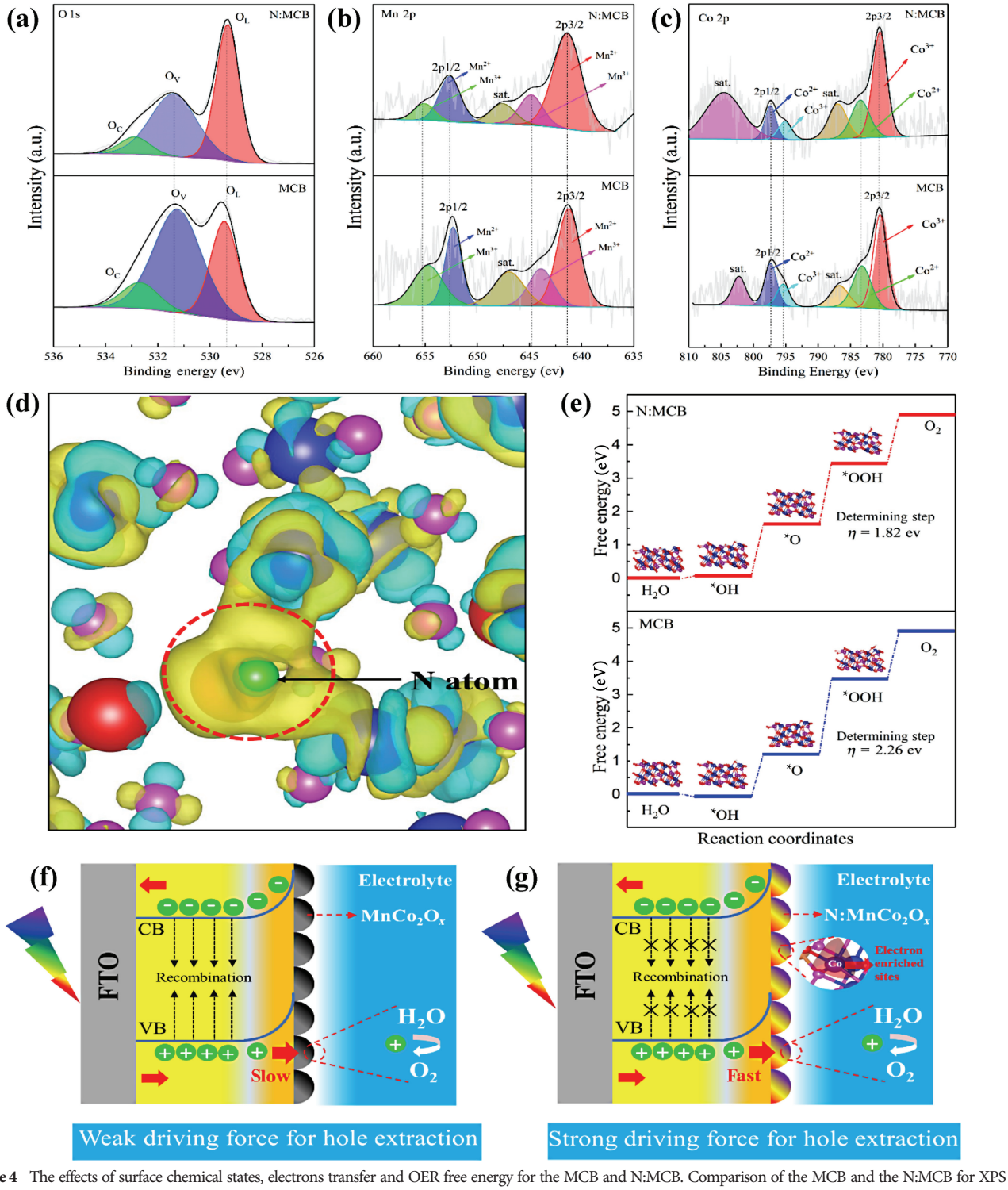

Figure 4 The effects of surface chemical states, electrons transfer and OER free energy for the MCB and N:MCB. Comparison of the MCB and the N:MCB for XPS spectra: (a) O 1s, (b) Mn 2p, and (c) Co 2p. (d) Schematic diagram of charge density difference (green is N atoms, blue is Co atoms, red is Mn atoms, and pink is O atoms), where the yellow regions represent the accumulation of electrons, and the blue regions represent the depletion of electrons. (e) Free energy change of MCB and N:MCB during OER. Mechanism illustration about hole extraction in (f) MCB and (g)N:MCB, respectively.

consistent with the XPS spectra. In addition, the Bader charge analysis is exhibited in Table S5 in the ESM, which confirms partial electrons enrich around the Co atoms, thereby promoting hole extraction from BVO for OER. To identify the effects of the increased electron density around Co atoms for OER activity, the free energy changes for the OER intermediates (OH*, O*, and OOH*) at the Co active sites of MCB and N:MCB are shown in Fig. 4(e). For MCB, the barrier energy of determining step is 2.26 eV at a process of forming the intermediate of OOH*, which is higher than that of N:MCB (1.82 eV), implying that the incorporation of N atoms into oxygen vacancy-rich $MnCo_2O_x$ can efficiently decrease the barrier energy for OER, and thereby enhancing PEC water splitting performance. Figs. 5(f) and 5(g) illustrate the significant influence of electron distribution tuning in the oxygen vacancy-rich $MnCo_2O_x$ OEC on hole extraction. Owing to the incorporation of low electronegative N atoms, the electron cloud is enriched at the Co active sites, providing strong driving force for the extraction of the photogenerated holes from BVO. Therefore, interfacial charge recombination is significantly suppressed, leading to the enhanced PEC water splitting performance.

To confirm the generic design of efficient OECs for PEC water

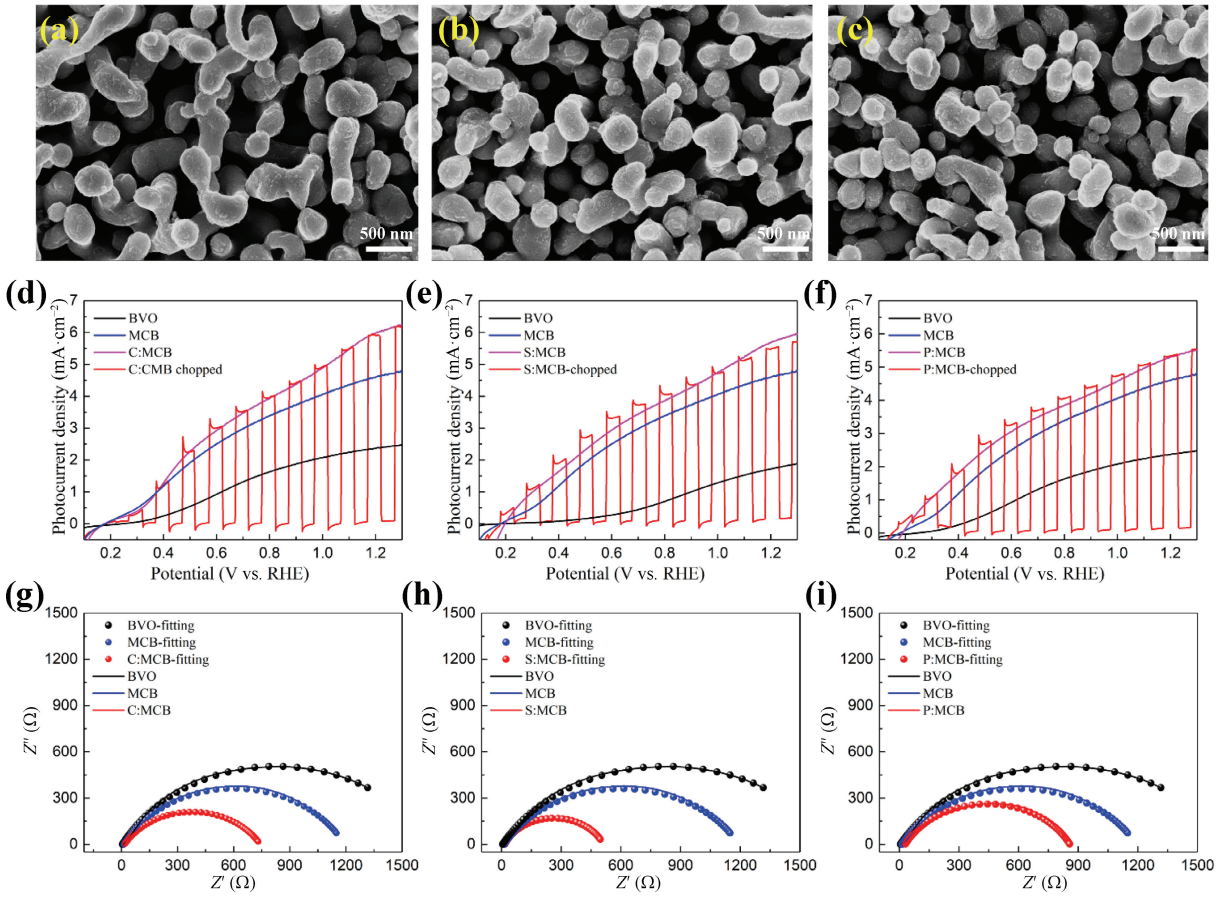

Figure 5 The SEM images and PEC performances of C:MCB, S:MCB, and P:MCB. The SEM images of the (a) C:MCB, (b) S:MCB, and (c) P:MCB. The LSV curves of the (d) C:MCB, (e) S:MCB, and (f) P:MCB and corresponding EIS results of the (g) C:MCB, (h) S:MCB, and (i) P:MCB.

oxidation through filling oxygen vacancies with heteroatoms. The PEC performances of MCB photoanodes filled with other low electronegative heteroatoms such as C, S, and P, were also investigated. As shown in Figs. 5(a)–5(c), all samples show similar morphologies. XPS spectra which were conducted to confirm the low electronegative heteroatoms (C, S, and P) are successfully incorporated in oxygen vacancy-rich $MnCo_2O_x$ OEC. As shown in Fig. S18 in the ESM, the increase binding C peak and characteristic peaks of P and S are observed, implying the existence of C, S, and P elements in the MCB photoanodes, respectively. As expected, the photocurrent densities of these low electronegative-heteroatom-filled photoanodes (denoted as C:MCB, S:MCB, and P:MCB) have significant enhancements compared to MCB (Figs. 5(d)–5(f)). Meanwhile, the corresponding EIS plots and fitted results are shown in Figs. 5(g)–5(i) and Table S6 in the ESM, respectively, confirming that the low electronegative element plays crucial roles in decreasing the interface (electrode surface/electrolyte) resistance. The above results illustrate that other low electronegative elements have a similar capability of tuning the electronic structure of $MnCo_2O_x$, and thereby further boosting the PEC water splitting performance of BVO photoanodes. It should be mentioned that careful modification is required to achieve the optimized PEC water splitting performance for C:MCB, S:MCB, and P:MCB.

4 Conclusions

In summary, we have reported a facile strategy to partly fill oxygen vacancies in MCB photoanodes with N atoms by a combined electrodeposition and sol-gel method. The N:MCB photoanode prepared by the optimized conditions exhibits an outstanding photocurrent density of 6.5 mA·cm^{-2} at 1.23 V_{RHE} under AM1.5 G illumination, and a high ABPE of 2.36% at a low applied potential of 0.62 V_{RHE}. In addition, the optimized N:MCB photoanode can stably deliver a photocurrent density of around 4.0 mA·cm^{-2} at 0.6 V_{RHE} under consecutive AM 1.5 G illumination for 150 h. A series of experimental characterizations and DFT analysis reveal that the improved stability and water oxidation activity are attributed to stable oxygen vacancy structure induced by the formed N–Mn bonds and modulated electron distribution due to the incorporation of N atoms. Low electronegative N atoms cause the enrichment of electrons at the Co active sites, promoting the extraction of photogenerated holes from BVO for OER. Furthermore, the free energy barrier of intermediates (OOH*) for OER processes significantly decreases from 2.26 to 1.82 eV due to the enriched electron distribution at the Co active sites, thereby accelerating the OER kinetics. This work provides an in-depth understanding for the design of highly active OECs applied in photoanodes for efficient PEC water splitting.

Acknowledgements

The authors would like to acknowledge the financial support from National Natural Science Foundation of China (No. 52002328), Shenzhen Science and Technology Program (No. JCYJ20220530161615035), the Practice and Innovation Funds for Graduate Students of Northwestern Polytechnical University (No. PF2023151), the Fundamental Research Funds for the Central Universities, and material characterizations from the Analytical & Testing Center of Northwestern Polytechnical University. L. Z. W. thanks the financial support of Australian Research Council through its Discovery Project (DP) and Laureate Fellowship.

Funding note: Open Access funding enabled and organized by CAUL and its Member Institutions.

Electronic Supplementary Material: Supplementary material (SEM images, XRD patterns, Photocurrent density measurements, CV curves, Raman spectroscopy curves, and XPS curves) is available in the online version of this article at https://doi.org/10.1007/s12274-023-5939-9.

References

[1] Yang, W.; Prabhakar, R. R.; Tan, J.; Tilley, S. D.; Moon, J. Strategies for enhancing the photocurrent, photovoltage, and stability of photoelectrodes for photoelectrochemical water splitting. *Chem. Soc. Rev.* **2019**, *48*, 4979–5015.

[2] Sun, K.; Kuang, Y. J.; Verlage, E.; Brunschwig, B. S.; Tu, C. W.; Lewis, N. S. Sputtered NiO_x films for stabilization of p^+n-InP photoanodes for solar-driven water oxidation. *Adv. Energy Mater.* **2015**, *5*, 1402276.

[3] Park, H. J.; Lee, H. J.; Kim, T. K.; Hong, S. H.; Wang, W. M.; Choi, T. J.; Kim, K. B. Formation of photo-reactive heterostructure from a multicomponent amorphous alloy with atomically random distribution. *J. Mater. Sci. Technol.* **2022**, *109*, 245–253.

[4] Kim, J. H.; Lee, J. S. Elaborately modified $BiVO_4$ photoanodes for solar water splitting. *Adv. Mater.* **2019**, *31*, 1806938.

[5] Wang, F.; Zhang, J. T.; Jin, C. C.; Ke, X. C.; Wang, F. F.; Liu, D. M. Unveiling the effect of crystal facets on piezo-photocatalytic activity of $BiVO_4$. *Nano Energy* **2022**, *101*, 107573.

[6] Lei, W. Y.; Zhou, T.; Pang, X.; Xue, S. X.; Xu, Q. L. Low-dimensional MXenes as noble metal-free co-catalyst for solar-to-fuel production: Progress and prospects. *J. Mater. Sci. Technol.* **2022**, *114*, 143–164.

[7] Lamers, M.; Li, W. J.; Favaro, M.; Starr, D. E.; Friedrich, D.; Lardhi, S.; Cavallo, L.; Harb, M.; Van De Krol, R.; Wong, L. H. et al. Enhanced carrier transport and bandgap reduction in sulfur-modified $BiVO_4$ photoanodes. *Chem. Mater.* **2018**, *30*, 8630–8638.

[8] Wang, S. C.; He, T. W.; Chen, P.; Du, A. J.; Ostrikov, K.; Huang, W.; Wang, L. Z. *In situ* formation of oxygen vacancies achieving near-complete charge separation in planar $BiVO_4$ photoanodes. *Adv. Mater.* **2020**, *32*, 2001385.

[9] Park, Y.; McDonald, K. J.; Choi, K. S. Progress in bismuth vanadate photoanodes for use in solar water oxidation. *Chem. Soc. Rev.* **2013**, *42*, 2321–2337.

[10] Liang, X. Z.; Wang, P.; Tong, F. X.; Liu, X. L.; Wang, C.; Wang, M. R.; Zhang, Q. Q.; Wang, Z. Y.; Liu, Y. Y.; Zheng, Z. K. et al. Bias-free solar water splitting by tetragonal zircon $BiVO_4$ nanocrystal photocathode and monoclinic scheelite $BiVO_4$ nanoporous photoanode. *Adv. Funct. Mater.* **2021**, *31*, 2008656.

[11] Jin, B. J.; Cho, Y.; Park, C.; Jeong, J.; Kim, S.; Jin, J.; Kim, W.; Wang, L. Y.; Lu, S. Y.; Zhang, S. L. et al. A two-photon tandem black phosphorus quantum dot-sensitized $BiVO_4$ photoanode for solar water splitting. *Energy Environ. Sci.* **2022**, *15*, 672–679.

[12] Gao, G. D.; Chen, R.; Wang, Q. J.; Cheung, D. W. F.; Zhao, J.; Luo, J. S. $NdCo_3$ molecular catalyst coupled with a $BiVO_4$ photoanode for photoelectrochemical water splitting. *ACS Appl. Energy Mater.* **2023**, *6*, 4027–4034.

[13] Gao, L. L.; Long, X. F.; Wei, S. Q.; Wang, C. L.; Wang, T.; Li, F.; Hu, Y. P.; Ma, J. T.; Jin, J. Facile growth of $AgVO_3$ nanoparticles on Mo-doped $BiVO_4$ film for enhanced photoelectrochemical water oxidation. *Chem. Eng. J.* **2019**, *378*, 122193.

[14] Xiong, B.; Wu, Y. T.; Du, J. Y.; Li, J.; Liu, B. Y.; Ke, G. L.; He, H. C.; Zhou, Y. $Cu_3Mo_2O_9$/$BiVO_4$ heterojunction films with integrated thermodynamic and kinetic advantages for solar water oxidation. *ACS Sustainable Chem. Eng.* **2020**, *8*, 14082–14090.

[15] Ta, C. X. M.; Akamoto, C.; Furusho, Y.; Amano, F. A macroporous-structured WO_3/Mo-doped $BiVO_4$ photoanode for vapor-fed water splitting under visible light irradiation. *ACS Sustainable Chem. Eng.* **2020**, *8*, 9456–9463.

[16] Zhang, W.; Tian, M.; Jiao, H. M.; Jiang, H. Y.; Tang, J. W. Conformal $BiVO_4$/WO_3 nanobowl array photoanode for efficient photoelectrochemical water splitting. *Chin. J. Catal.* **2022**, *43*, 2321–2331.

[17] Yang, L. Q.; Song, X.; Yu, J. S.; Wang, H. T.; Zhang, Z. H.; Geng, R. Y.; Cao, J. R.; Baran, D.; Tang, W. H. Tuning of the conformation of asymmetric nonfullerene acceptors for efficient organic solar cells. *J. Mater. Chem. A* **2019**, *7*, 22279–22286.

[18] Mohamed, N. A.; Arzaee, N. A.; Mohamad Noh, M. F.; Ismail, A. F.; Safaei, J.; Sagu, J. S.; Johan, M. R.; Mat Teridi, M. A. Electrodeposition of $BiVO_4$ with needle-like flower architecture for high performance photoelectrochemical splitting of water. *Ceram. Int.* **2021**, *47*, 24227–24239.

[19] Liu, B. Y.; Wang, X.; Zhang, Y. J.; Xu, L. C.; Wang, T. S.; Xiao, X.; Wang, S. C.; Wang, L. Z.; Huang, W. A $BiVO_4$ photoanode with a VO_x layer bearing oxygen vacancies offers improved charge transfer and oxygen evolution kinetics in photoelectrochemical water splitting. *Angew. Chem., Int. Ed.* **2023**, *62*, e202217346.

[20] Gao, R. T.; Nguyen, N. T.; Nakajima, T.; He, J. L.; Liu, X. H.; Zhang, X. Y.; Wang, L.; Wu, L. M. Dynamic semiconductor-electrolyte interface for sustainable solar water splitting over 600 hours under neutral conditions. *Sci. Adv.* **2023**, *9*, eade4589.

[21] Gao, R. T.; He, D.; Wu, L. J.; Hu, K.; Liu, X. H.; Su, Y. G.; Wang, L. Towards long-term photostability of nickel hydroxide/$BiVO_4$ photoanodes for oxygen evolution catalysts via *in situ* catalyst tuning. *Angew. Chem., Int. Ed.* **2020**, *59*, 6213–6218.

[22] Gao, R. T.; Wang, L. Stable cocatalyst-free $BiVO_4$ photoanodes with passivated surface states for photocorrosion inhibition. *Angew. Chem., Int. Ed.* **2020**, *59*, 23094–23099.

[23] Zhang, Y. J.; Xu, L. C.; Liu, B. Y.; Wang, X.; Wang, T. S.; Xiao, X.; Wang, S. C.; Huang, W. Engineering $BiVO_4$ and oxygen evolution cocatalyst interfaces with rapid hole extraction for photoelectrochemical water splitting. *ACS Catal.* **2023**, *13*, 5938–5948.

[24] Wang, S. C.; He, T. W.; Yun, J. H.; Hu, Y. X.; Xiao, M.; Du, A. J.; Wang, L. Z. New Iron-cobalt oxide catalysts promoting $BiVO_4$ films for photoelectrochemical water splitting. *Adv. Funct. Mater.* **2018**, *28*, 1802685.

[25] Wang, S. C.; Liu, B. Y.; Wang, X.; Zhang, Y. J.; Huang, W. Nanoporous MoO_{3-x}/$BiVO_4$ photoanodes promoting charge separation for efficient photoelectrochemical water splitting. *Nano Res.* **2022**, *15*, 7026–7033.

[26] Wang, Q. J.; Wu, L. X.; Zhang, Z.; Cheng, J. S.; Chen, R.; Liu, Y.; Luo, J. S. Elucidating the role of hypophosphite treatment in enhancing the performance of $BiVO_4$ photoanode for photoelectrochemical Water Oxidation. *ACS Appl. Mater. Interfaces* **2022**, *14*, 26642–26652.

[27] Zhang, B. B.; Wang, L.; Zhang, Y. J.; Ding, Y.; Bi, Y. P. Ultrathin FeOOH nanolayers with abundant oxygen vacancies on $BiVO_4$ photoanodes for efficient water oxidation. *Angew. Chem., Int. Ed.* **2018**, *57*, 2248–2252.

[28] Dong, G. J.; Hu, H. Y.; Huang, X. J.; Zhang, Y. J.; Bi, Y. P. Rapid activation of Co_3O_4 cocatalysts with oxygen vacancies on TiO_2 photoanodes for efficient water splitting. *J. Mater. Chem. A* **2018**, *6*, 21003–21009.

[29] Wei, Y.; Liao, A.; Zhou, Y.; Zou, Z. Enhancing the water splitting performance via decorating Fe_2O_3 nanoarrays with oxygen-vacancy-rich $Ni_{1-x}Fe_xS$ electrocatalyst. *Mater. Today Phys.* **2021**, *16*, 100317.

[30] Wei, A. M.; Deng, J. J.; Lu, C.; Wang, H.; Yang, B.; Zhong, J.

$Fe_2(MoO_4)_3$ modified hematite with oxygen vacancies for high-efficient water oxidation. *Chem. Eng. J.* **2020**, *395*, 125127.
[31] Xiao, Z. H.; Wang, Y.; Huang, Y. C.; Wei, Z. X.; Dong, C. L.; Ma, J. M.; Shen, S. H.; Li, Y. F.; Wang, S. Y. Filling the oxygen vacancies in Co_3O_4 with phosphorus: An ultra-efficient electrocatalyst for overall water splitting. *Energy Environ. Sci.* **2017**, *10*, 2563–2569.
[32] Kim, T. W.; Choi, K. S. Nanoporous $BiVO_4$ photoanodes with dual-layer oxygen evolution catalysts for solar water splitting. *Science* **2014**, *343*, 990–994.
[33] Zhao, L.; Wei, J. D.; Li, Y. T.; Han, C.; Pan, L.; Liu, Z. F. Photoelectrochemical performance of W-doped $BiVO_4$ photoanode. *J. Mater. Sci. :Mater. Electron.* **2019**, *30*, 21425–21434.
[34] Cheng, J.; Yan, X. L.; Mo, Q. H.; Liu, B. T.; Wang, J.; Yang, X.; Li, L. Facile synthesis of g-C_3N_4/$BiVO_4$ heterojunctions with enhanced visible light photocatalytic performance. *Ceram. Int.* **2017**, *43*, 301–307.
[35] Zheng, G. W.; Wang, J. S.; Zu, G. N.; Che, H. B.; Lai, C.; Li, H. Y.; Murugadoss, V.; Yan, C.; Fan, J. C.; Guo, Z. H. Sandwich structured WO_3 nanoplatelets for highly efficient photoelectrochemical water splitting. *J. Mater. Chem. A* **2019**, *7*, 26077–26088.
[36] Zhou, T. S.; Wang, J. C.; Chen, S.; Bai, J.; Li, J. H.; Zhang, Y.; Li, L. S.; Xia, L. G.; Rahim, M.; Xu, Q. J. et al. Bird-nest structured ZnO/TiO_2 as a direct Z-scheme photoanode with enhanced light harvesting and carriers kinetics for highly efficient and stable photoelectrochemical water splitting. *Appl. Catal. B Environ.* **2020**, *267*, 118599.
[37] Sheng, S.; Ye, K.; Gao, Y. Y.; Zhu, K.; Yan, J.; Wang, G. L.; Cao, D. X. Simultaneously boosting hydrogen production and ethanol upgrading using a highly-efficient hollow needle-like copper cobalt sulfide as a bifunctional electrocatalyst. *J. Colloid Interface Sci.* **2021**, *602*, 325–333.
[38] Kahraman, A.; Barzgar Vishlaghi, M.; Baylam, I.; Sennaroglu, A.; Kaya, S. Roles of charge carriers in the excited state dynamics of $BiVO_4$ photoanodes. *J. Phys. Chem. C* **2019**, *123*, 28576–28583.
[39] Abdi, F. F.; Savenije, T. J.; May, M. M.; Dam, B.; Van De Krol, R. The origin of slow carrier transport in $BiVO_4$ thin film photoanodes: A time-resolved microwave conductivity study. *J. Phys. Chem. Lett.* **2013**, *4*, 2752–2757.
[40] Soltani, T.; Tayyebi, A.; Lee, B. K. $BiFeO_3$/$BiVO_4$ p-n heterojunction for efficient and stable photocatalytic and photoelectrochemical water splitting under visible-light irradiation. *Catal. Today* **2020**, *340*, 188–196.
[41] Kresse, G.; Furthmüller, J. Efficiency of *ab-initio* total energy calculations for metals and semiconductors using a plane-wave basis set. *Comput. Mater. Sci.* **1996**, *6*, 15–50.
[42] Perdew, J. P.; Burke, K.; Ernzerhof, M. Generalized gradient approximation made simple. *Phys. Rev. Lett.* **1996**, *77*, 3865–3868.
[43] Blöchl, P. E. Projector augmented-wave method. *Phys. Rev. B* **1994**, *50*, 17953–17979.
[44] Grimme, S.; Antony, J.; Ehrlich, S.; Krieg, H. A consistent and accurate *ab initio* parametrization of density functional dispersion correction (DFT-D) for the 94 elements H-Pu. *J. Chem. Phys.* **2010**, *132*, 154104.
[45] Zhou, Z. M.; Chen, J. J.; Wang, Q. L.; Jiang, X. X.; Shen, Y. Enhanced photoelectrochemical water splitting using a cobalt-sulfide-decorated $BiVO_4$ photoanode. *Chin. J. Catal.* **2022**, *43*, 433–441.
[46] Zhang, Y.; Bai, J.; Wang, J. C.; Chen, S.; Zhu, H.; Li, J. H.; Li, L. S.; Zhou, T. S.; Zhou, B. X. *In-situ* and synchronous generation of oxygen vacancies and FeO_x OECs on $BiVO_4$ for ultrafast electron transfer and excellent photoelectrochemical performance. *Chem. Eng. J.* **2020**, *401*, 126134.
[47] Wang, Y. L.; Yu, D.; Wang, W.; Gao, P.; Zhong, S.; Zhang, L. S.; Zhao, Q. Q. Synthesizing Co_3O_4-$BiVO_4$/g-C_3N_4 heterojunction composites for superior photocatalytic redox activity. *Sep. Purif. Technol.* **2020**, *239*, 116562.
[48] He, B.; Zhao, F. F.; Yi, P.; Huang, J.; Wang, Y.; Zhao, S. Q.; Li, Z.; Zhao, Y. L.; Liu, X. Q. Spinel-oxide-integrated $BiVO_4$ photoanodes with photothermal effect for efficient solar water oxidation. *ACS Appl. Mater. Interfaces* **2021**, *13*, 48901–48912.
[49] Lin, Y. C.; Hsu, L. C.; Lin, C. Y.; Chiang, C. L.; Chou, C. M.; Wu, W. W.; Chen, S. Y.; Lin, Y. G. Sandwich-nanostructured n-Cu_2O/AuAg/p-Cu_2O photocathode with highly positive onset potential for improved water reduction. *ACS Appl. Mater. Interfaces* **2019**, *11*, 38625–38632.
[50] Di, T. M.; Deng, Q. R.; Wang, G. M.; Wang, S. G.; Wang, L. X.; Ma, Y. H. Photodeposition of CoO_x and MoS_2 on CdS as dual cocatalysts for photocatalytic H_2 production. *J. Mater. Sci. Technol.* **2022**, *124*, 209–216.
[51] Omar, M. M.; Fawzy, S. M.; El-Shabasy, A. B.; Allam, N. K. Large-diameter light-scattering complex multipodal nanotubes with graded refractive index: Insights into their Formation mechanism and photoelectrochemical performance. *J. Mater. Chem. A* **2017**, *5*, 23600–23611.
[52] Ouyang, T.; Wang, X. T.; Mai, X. Q.; Chen, A. N.; Tang, Z. Y.; Liu, Z. Q. Coupling magnetic single-crystal $Co_2Mo_3O_8$ with ultrathin nitrogen-rich carbon layer for oxygen evolution reaction. *Angew. Chem., Int. Ed.* **2020**, *59*, 11948–11957.
[53] Wang, S. C.; Li, Y. L.; Wang, X.; Zi, G. H.; Zhou, C. Y.; Liu, B. Y.; Liu, G.; Wang, L. Z.; Huang, W. One-step supramolecular preorganization constructed crinkly graphitic carbon nitride nanosheets with enhanced photocatalytic activity. *J. Mater. Sci. Technol.* **2022**, *104*, 155–162.
[54] Gu, S. N.; Li, W. J.; Wang, F. Z.; Wang, S. Y.; Zhou, H. L.; Li, H. D. Synthesis of buckhorn-like $BiVO_4$ with a shell of CeO_x nanodots: Effect of heterojunction structure on the enhancement of photocatalytic activity. *Appl. Catal. B Environ.* **2015**, *170–171*, 186–194.
[55] Huang, S. F.; Tie, D.; Wang, M.; Wang, B.; Jia, P.; Wang, Q. J.; Chang, G. L.; Zhang, J. J.; Zhao, Y. F. Largely increased lithium storage ability of mangnese oxide through a continuous electronic structure modulation and elevated capacitive contribution. *ACS Sustainable Chem. Eng.* **2019**, *7*, 740–747.
[56] Wang, X. R.; Liu, J. Y.; Liu, Z. W.; Wang, W. C.; Luo, J.; Han, X. P.; Du, X. W.; Qiao, S. Z.; Yang, J. Identifying the key role of pyridinic-N-Co bonding in synergistic electrocatalysis for reversible ORR/OER. *Adv. Mater.* **2018**, *30*, 1800005.
[57] Zhang, C. Y.; Kong, J. F.; Wang, F. C.; Zou, J.; Huang, Y. Q. Preparation of ferromagnetic N-Mn codoped ZnO thin films by ultrasonic spray pyrolysis. *J. Mater. Sci. :Mater. Electron.* **2017**, *28*, 426–434.